JOURNAL OF GEOPHYSICAL RESEARCH, VOL. 99, NO. D12, PAGES 25,891–25,901, DECEMBER 20, 1994

Relationship between clear-sky atmospheric greenhouse effect and deep convection during the Central Equatorial Pacific Experiment: Model calculations and satellite observations

C. P. Weaver and W. D. Collins[1]
Center for Clouds, Chemistry and Climate, Scripps Institution of Oceanography, La Jolla, California

H. Grassl
Max Planck Institute for Meteorology, Mainz, Germany

Abstract. This study investigates the relation between tropical convection and the atmospheric greenhouse effect using data collected during the Central Equatorial Pacific Experiment (CEPEX). We present calculations of total clear-sky greenhouse effect and its partitioning between the lower, middle, and upper troposphere using high-quality balloon soundings of temperature and humidity as input to a radiative transfer model. The soundings were taken from a ship every 6 hours from March 7 to 20, 1993, in the central Pacific. We examine the influence on atmospheric greenhouse effect due to changes in humidity and lapse rate and investigate the relationship between atmospheric greenhouse effect, water vapor, and deep convection. Our observations indicate that periods of active or suppressed convection with timescales of the order of days can produce large spatial gradients in clear-sky atmospheric greenhouse trapping in warm, climatologically convective regions. While the sea surface temperature (SST) decreased by 2 K from west to east, temperatures above 850 mbar showed considerably less variation. Accordingly, lapse rate changes occurred primarily in the boundary layer and such changes account for 80% of the gradient in boundary layer greenhouse effect. The column-integrated water vapor content from the surface to 850 mbar was nearly constant in each of the regimes. Conversely, large variations in column-integrated water vapor above 850 mbar and particularly above 500 mbar account for nearly all the gradient in the greenhouse effect in the middle and upper troposphere. Coincident outgoing longwave radiation (OLR) analyses derived from satellite observations show active deep convection in areas with high clear-sky greenhouse trapping and upper level moisture and generally clear, suppressed conditions elsewhere. In addition, the surface net flux and outgoing flux emitted to space decreased with increased SST. The reduced cooling of the ocean-atmosphere system is consistent with a supergreenhouse effect operating in regions of deep convection.

1. Introduction

The interaction between water vapor and climate is a key issue in the global change debate. *Manabe and Wetherald* [1967] showed that water vapor feedback could increase the sea surface temperature (SST) response to a change in radiative forcing by approximately a factor of 2. In the past few years, several studies have given close attention to the role of water vapor and water vapor feedbacks in determining atmospheric longwave trapping. In particular, investigators have attacked the problem using satellite observations [*Raval and Ramanathan*, 1989; *Rind et al.*, 1991; *Stephens and Greenwald*, 1991; *Kiehl and Briegleb*, 1992; *Slingo and Webb*, 1992; *Webb et al.*, 1993] and radiation model calculations [*Kiehl and Briegleb*, 1992; *Slingo and Webb*, 1992; *Minschwaner and McElroy*, 1992; *Hallberg and Inamdar*, 1993]. *Raval and Ramanathan* [1989], *Stephens and Greenwald* [1991], and *Webb et al.* [1993] use monthly mean data from the Earth Radiation Budget Experiment (ERBE) to derive a strong relationship between column water vapor and the clear-sky atmospheric greenhouse effect. We have defined the clear-sky atmospheric greenhouse effect (G_a) in the following manner:

$$G_a = F^+_{\text{surf}} - F^+_{\text{toa}} \tag{1}$$

F^+_{surf} is the upwelling longwave flux at the surface, defined as $\sigma(\text{SST})^4$ where σ is the Stefan-Boltzmann constant, and F^+_{toa} is the outgoing longwave flux at the top of the atmosphere. This definition of G_a is not universal (e.g., *Stephens and Greenwald* [1991] have used a different definition), but we have adopted it for this study. *Kiehl and Briegleb* [1992] use the NCAR community climate model to show that clear-sky outgoing longwave flux in the tropics can decrease by as much as 35 W m^{-2} due to a twofold increase in column water

[1]Also at California Space Institute, Scripps Institution of Oceanography, La Jolla, California.

Paper number 94JD02323.
0148-0227/94/94JD-02323$05.00

vapor associated with the onset of a deep convective event. Central to these studies is the influence of deep convective activity in the tropics on G_a.

Ramanathan and Collins [1991], using monthly mean observations of the 1987 El Niño taken as part of ERBE, have found that much of the warmest tropical ocean is unstable with respect to cooling by longwave radiation, a phenomenon known as the "supergreenhouse effect." In other words, the increase in G_a with SST is greater than the corresponding increase in surface emission. The onset of the supergreenhouse effect coincides with the threshold temperature for deep convection of 300 to 301 K proposed by *Gadgil et al.* [1984] and *Graham and Barnett* [1987]. *Inamdar and Ramanathan* [1994] use ship soundings from the period 1985 to 1989 in conjunction with radiation model calculations to compare vertical water vapor distribution and G_a between regions with SST below and above this threshold. They found a sharp increase in low-level water vapor concentration and G_a with SST, particularly at SST higher than approximately 300 K. Their calculated average increase in G_a from climatologically convective to nonconvective profiles of 6.9 W m^{-2} K^{-1} is greater than the increase in surface emission with temperature (approximately 6 W m^{-2} K^{-1} at 300 K). Exploring the nature of the supergreenhouse effect and the effect of deep convection on atmospheric trapping of longwave radiation was a goal of the Central Equatorial Pacific Experiment (CEPEX) conducted in the spring of 1993.

The primary goal of this paper is to focus on regions where the surface temperature is everywhere above the threshold for deep convection. Both spatial correlation of monthly mean G_a with SST and temporal correlation of interannual variations of monthly mean G_a with SST indicate a supergreenhouse effect, $dG_a/d\mathrm{SST} > 6.5$ W m^{-2} K^{-1}. It has been shown [*Minschwaner and McElroy*, 1992; *Hallberg and Inamdar*, 1993] that to produce a supergreenhouse effect, increases in absolute humidity with SST are required that are far beyond the thermodynamic dependence of water vapor concentration on temperature in a fixed relative humidity system. This is in contrast to the region below the threshold temperature for deep convection where the coupling between G_a and water vapor is governed by the Clausius-Clapeyron relation. The fundamental question is: what processes contribute to the moistening of the atmosphere over warm oceans? An obvious candidate is deep convection. If we can link the supergreenhouse effect with pronounced moistening of the troposphere and if we can in turn link this moistening with deep convection, then we are somewhat closer to providing a fundamental understanding of the correlations obtained from satellite studies. The previous studies suggest that the variation of G_a with SST can be expanded as a sum of partial derivatives. Mathematically, let us define, on monthly or longer timescales, with q representing absolute humidity, Γ representing lapse rate, and T = SST:

$$\frac{dG_a}{dT} = \frac{\partial G_a}{\partial T} + \frac{\partial G_a}{\partial q}\frac{dq}{dT} + \frac{\partial G_a}{\partial \Gamma}\frac{d\Gamma}{dT} \tag{2}$$

It will be shown below that the contribution of changes in lapse rate to changes in G_a are important in the boundary layer, but small elsewhere. Studies of the supergreenhouse effect indicate that above the threshold temperature for deep convection, the local change in water vapor due to the Clausius-Clapeyron relation is insufficient to explain observed water vapor increases. Therefore let us write

$$\frac{dq}{dT} = \frac{\partial q}{\partial T} + \frac{\partial q}{\partial C}\frac{dC}{dT} \tag{3}$$

C is an index for deep convection such as outgoing longwave radiation (OLR). The second term on the right represents the moistening effect of deep convection scaled by the frequency of deep convection as a function of SST. The local effect of changes in SST, $\partial G_a/\partial T$, which depends on the increase in surface emission with increasing SST due to the Stefan-Boltzmann relation, as well as $\partial q/\partial T$, has been shown to be insufficient to produce a supergreenhouse effect [*Hallberg and Inamdar*, 1993], though $\partial G_a/\partial T$ does contribute to our observed gradients. In this investigation we are interested in $\partial G_a/\partial q$ and $\partial q/\partial C$, since the determination of dC/dT is beyond the scope of the CEPEX sample.

This study uses radiation model calculations employing in situ vertical soundings of temperature and water vapor taken during CEPEX. One of the advantages of performing clear-sky radiation calculations with soundings taken in clear and cloudy conditions is that one can avoid certain potential biases inherent in G_a estimates from satellite data [*Raval and Ramanathan*, 1989; *Ramanathan and Collins*, 1991]. In this study, satellite data are used to determine the spatial and temporal relationship between the soundings and the synoptic-scale convective activity. We present satellite observations from the Japanese meteorological satellite GMS 4 as well as NMC pentad outgoing longwave radiation (OLR) analyzed fields, spatially and temporally colocated with the balloon soundings. This study shows that large variations in G_a are possible even throughout an area which is potentially convective everywhere (SST > 300 K) and that such variations depend on proximity in space and time to individual deep convective episodes.

Section 2 provides a description of the radiation code as well as the water vapor and temperature soundings. Section 3 seeks to establish the connection between enhanced upper level water vapor and deep convection. Section 4 extends this connection to derived quantities such as G_a, surface fluxes, and atmospheric heating tendencies. Section 5 is summary and discussion.

2. Method

Model

For the radiation calculations this study uses a version of the LOWTRAN 7 code at 20 cm^{-1} resolution [*Kneizys et al.*, 1988]. The continuum parameters are those used in LOWTRAN 6. There are 53 vertical levels with a typical thickness of 20 mbar from the surface to the top of the atmosphere (TOA). The internal resolution of the radiative transfer calculation is 1 mbar. The model includes contributions from water vapor (including temperature-dependent continuum absorption), carbon dioxide, ozone, methane, and nitrous oxide. The trace gas data are from the McClatchey standard tropical atmosphere. Computed fluxes from LOWTRAN 7 agree to within 3 W m^{-2} with those from line-by-line calculations [*Ellingson et al.*, 1991] and to within 5 W m^{-2} with colocated surface pyrgeometer measurements [*Dutton*, 1993].

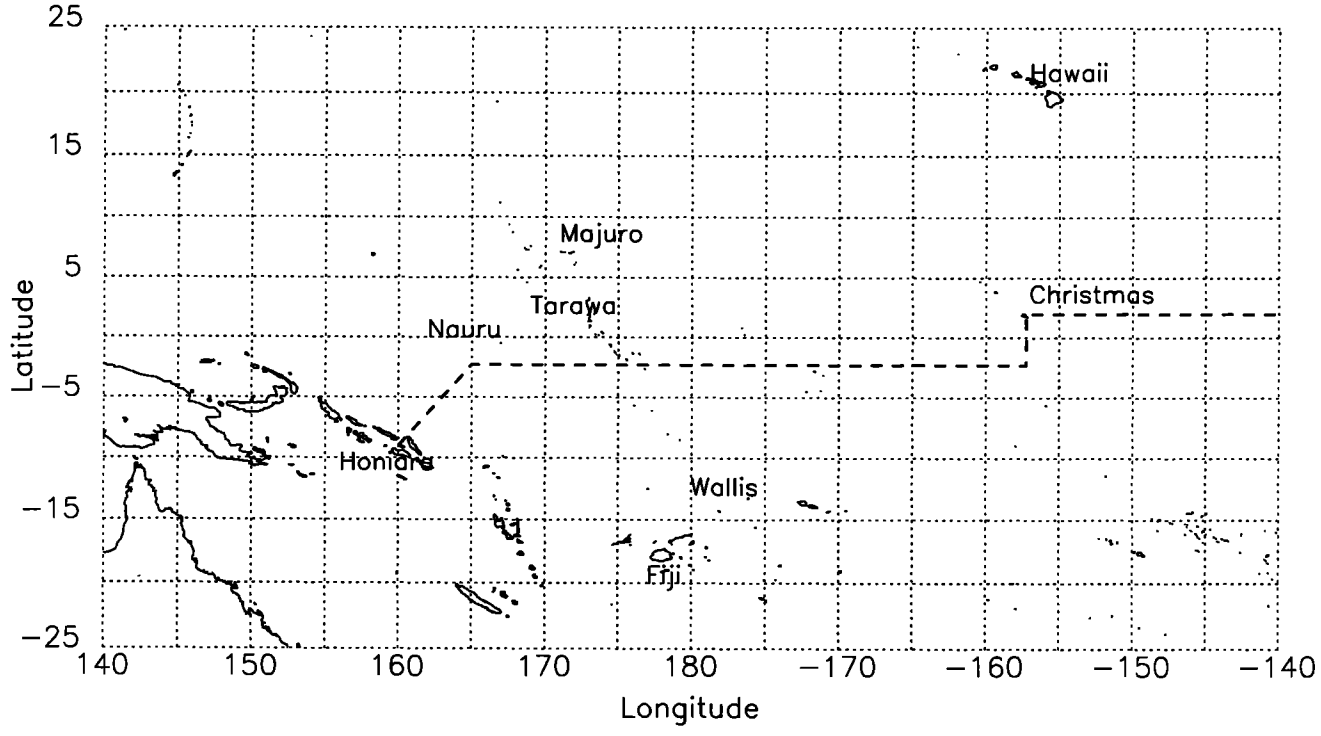

Figure 1. Map of the Central Equatorial Pacific Experiment (CEPEX) region showing the track of the R/V *Vickers* (dashed triple-dotted line from Honiara to Christmas Island and beyond).

Water Vapor and Temperature Profiles

The calculations in section 4 use vertical soundings of water vapor and temperature from Vaisala upsondes as input to the radiation code. The upsondes are accurate to 1 mbar in pressure, 1 K in temperature, and 5% in relative humidity up to approximately 250 mbar and are probably accurate within 10% at altitudes between 250 mbar and approximately 150 mbar [*Kley et al.*, 1993]. The soundings represent a high-quality water vapor and temperature data set for the middle and upper troposphere. There is some evidence that these soundings are dry by up to 10% relative humidity in the boundary layer (S. Sherwood, personal communication, 1993). One of us (H. Grassl) is currently investigating this possibility. A uniform increase of 10% in mixing ratio from the surface to 850 mbar changes the calculated G_a values by less than 1 W m^{-2} and changes the surface downwelling flux values by approximately 5 W m^{-2}.

The soundings were launched 4 times daily (0000, 0006, 1200, and 1800 UT) from the R/V *John Vickers* during CEPEX. The model profiles consist of standard climatological values above approximately 120 mbar. The results in this study are based upon 46 soundings covering the period March 7–20, 1993 (UT) as the ship proceeded primarily at 2° south of the equator from Honiara to Christmas Island (Figure 1).

All the soundings were averaged to create mean temperature and water vapor profiles. These mean profiles were used to construct two additional sets of soundings: one with a mean temperature profile (including a mean SST of 301.7 K) and individual mixing ratio profiles and one with a mean mixing ratio profile and individual temperature profiles (including individual SSTs). This paper will refer to the three sets of profiles as standard, fixed temperature, and fixed water vapor, respectively. The current study uses these three sets to identify contributions to the gradient in greenhouse effect across the CEPEX region from water vapor and lapse rate gradients. In particular, we have divided the atmosphere into three regions: surface to 850 mbar, 850 to 500 mbar, and 500 to 200 mbar to investigate the relative roles of water vapor and lapse rate gradients in the lower, middle, and upper troposphere.

3. Relation of Atmospheric Humidity to Convection

Observed Sea Surface Temperature (SST) and Water Vapor

Figure 2 shows the SST variation for all the soundings used in this study. These are temperatures from the National Meteorological Center (NMC) blended analysis [*Reynolds*, 1988] for each day corresponding to a balloon launch. The total range is of the order of 2 K. It is notable that the minimum SST is above 300 K. We have compared the NMC SSTs with the Vickers 3-m-depth ship-intake temperatures and have found excellent agreement between the two. Over the 46-sounding launch period the mean difference between the two is 0.04 K, while the rms difference is 0.31 K. The Vickers data are much noisier than the NMC data since it is sampled every 5 min. We have compared the LOWTRAN-derived radiometric quantities discussed in this paper calculated with NMC SSTs to those calculated with Vickers SSTs and have found insignificant differences between the two. The values reported here are those calculated with NMC SSTs.

Figures 3a and 3b show the variation in column water vapor across the CEPEX region calculated from the standard set of 46 soundings. The integral was computed by

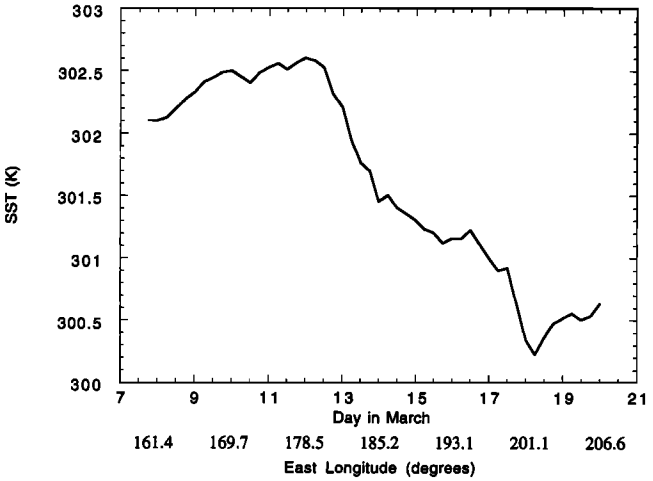

Figure 2. Variation of the National Meteorological Center (NMC) blended sea surface temperature (SST) analysis [*Reynolds*, 1988] along the track of the R/V *Vickers*.

summing over pressure levels. There is a large gradient from west to east which is due almost entirely to variation in the middle and upper troposphere. Though the absolute gradient is lower in the upper than in the middle troposphere, the upper tropospheric gradient represents a much higher percentage change (see *Shine and Sinha* [1991] for additional discussion of related points). Significant west-to-east gradients in water vapor mixing ratio are present at all levels between 500 and 200 mbar. It is interesting to note the group of points beginning between March 18 and 19 on each of the curves in Figures 3a and 3b. In the total, middle, and upper troposphere curves there is a sharp increase in column water vapor, reversing much of the west-to-east decrease. We will return to this below.

National Meteorological Center (NMC) Outgoing Longwave Radiation (OLR) and GMS 4 Observations

To establish a climatological context for the calculations of the following sections, Figure 4 shows NMC pentad OLR analyses for the dates immediately before, during, and immediately after the passage of the R/V *Vickers* through the CEPEX region. Refer to Figure 1 for the exact ship track. Contours with OLR < 240 W m^{-2} are represented by dashed curves.

The prevalence of deep convection is evident in regions of low (<200 W m^{-2}) values of OLR west of the dateline from March 7 to 11 as the *Vickers* proceeded from 160°E to 177°E. From March 12 to 16 the *Vickers* proceeded along the 2°S line from 178°E to 196°E under increasingly clear conditions characterized by OLR values ranging from 240 to 270 W m^{-2}.

For the period March 17–21 the *Vickers* was in the vicinity of Christmas Island (2°N, 202°E). The lower OLR values between 210 and 240 W m^{-2} correspond to an increase in convective activity. Recall from Figure 3b that the upper troposphere is significantly moister after 1200 UT on March 18 than in the previous soundings. Figure 4 shows active convection occurring at the position of the R/V *Vickers* for the first time on its course through the eastern half of the CEPEX region. This is correlated with strong increases in middle and upper tropospheric water vapor.

To use the observed GMS brightness temperatures to diagnose convection, we averaged the temperatures from the hourly satellite scan closest to each sounding launch time over a 10^4 km^2 block centered on the launch point. We also recorded the minimum brightness temperature within the block (Figure 5). The 100 km × 100 km region was used to account for drift in the balloon after launching. The sounding data and corresponding calculations were collected into two bins, one in which the 10^4 km^2 minimum brightness temperature was less than 250 K and one in which it was greater than or equal to 250 K. In this sample, temperatures less than 250 K usually indicate some convective cloud presence in the 10^4 km^2 region around the launch point. However, it is misleading to use infrared window brightness temperature alone as an index for convection, since one would observe similar temperatures from a case in which the scene was completely covered by high, thin cloud not associated with any deep convection and from a case in which half the scene was obscured by high, thick cloud associated with a deep convective system. For example, the cold points around

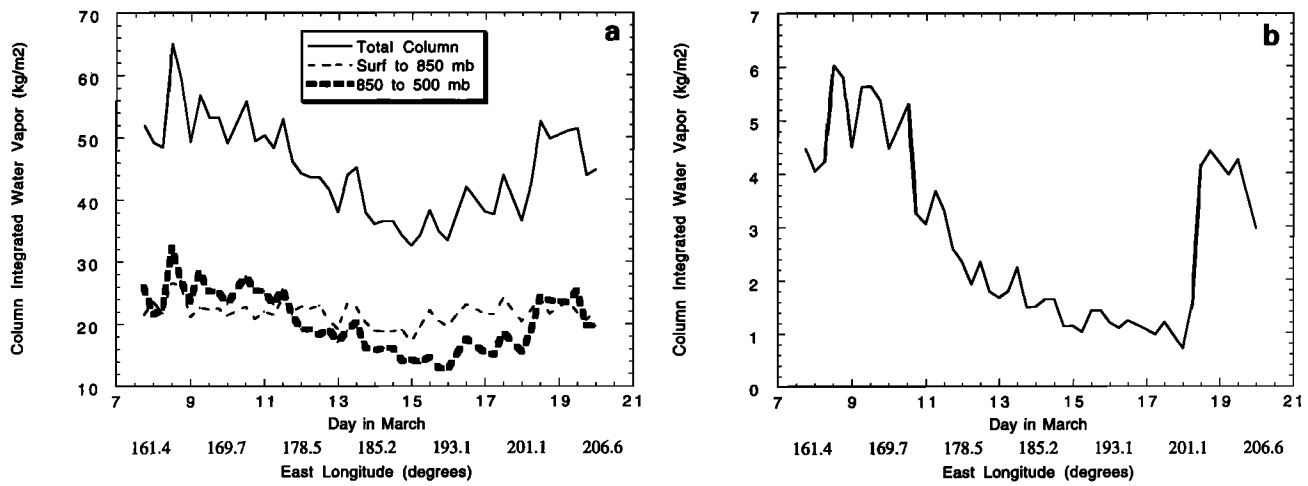

Figure 3. (a) Column-integrated water vapor in kilograms per square meter (kg m^{-2}) calculated using the Vaisala soundings. Total column (solid curve), surface to 850 mbar (thin dashed curve), and 850 to 500 mbar (thick dashed curve). (b) 500- to 200-mbar column-integrated water vapor in kg m^{-2}.

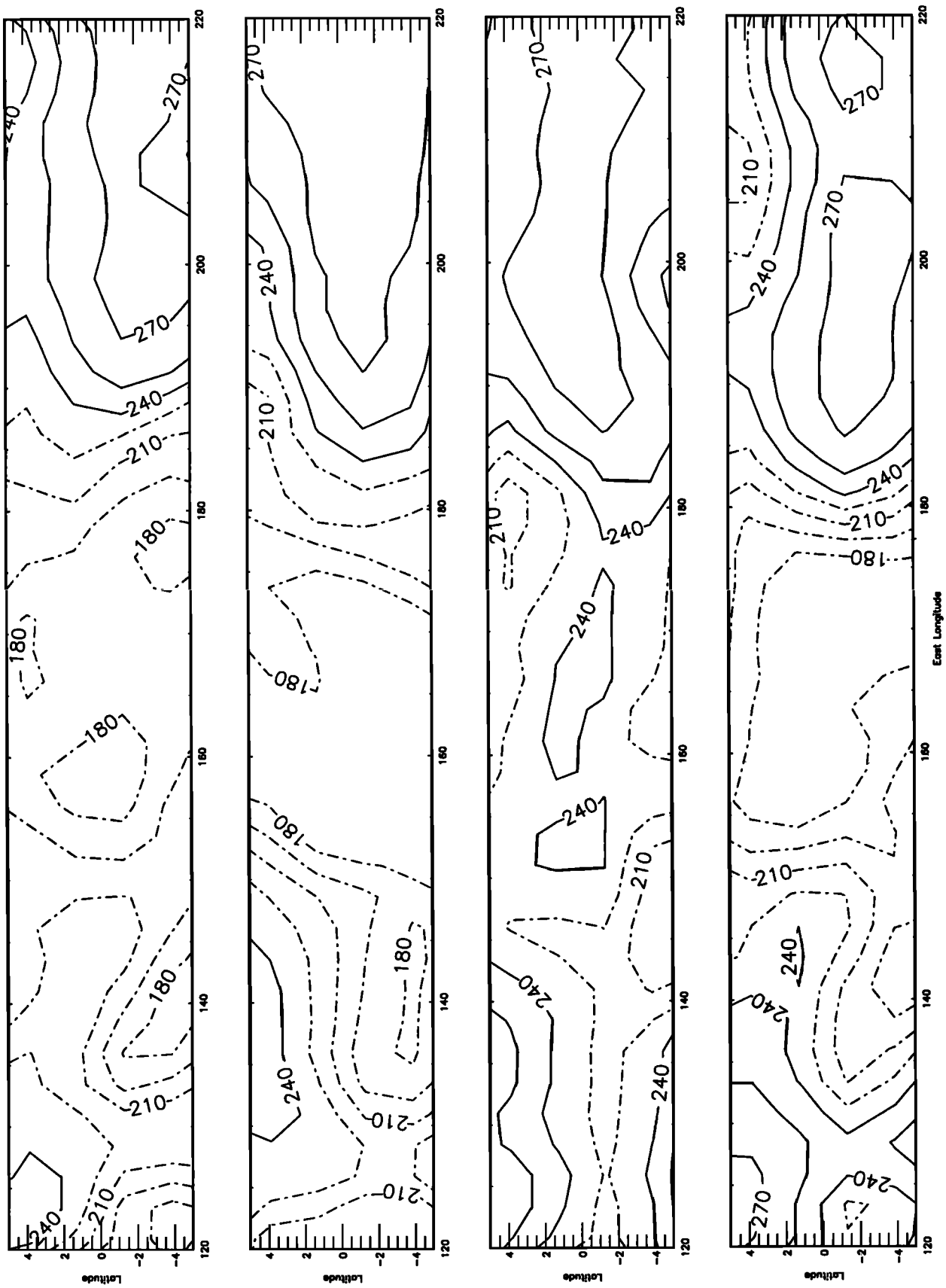

Figure 4. NMC pentad analyses of outgoing longwave radiation (OLR) in watts per square meter (W m^{-2}). The pentads displayed in sequence are March 2–6, 1993 (topmost), March 7–11, 1993, March 12–16, 1993, and March 17–21, 1993. The contour interval is 15 W m^{-2}. Contours less than 240 W m^{-2} are represented by dashed curves.

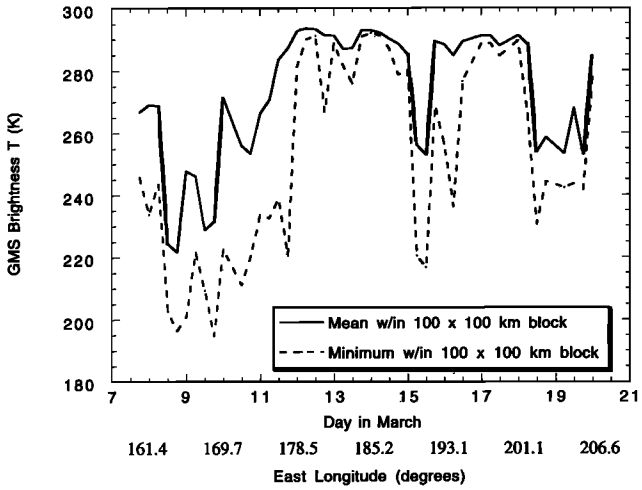

Figure 5. Mean and minimum GMS infrared window channel brightness temperature in K along the R/V *Vickers* ship track. Values are associated with a 10^4 km^2 region centered on the launch point of each sounding.

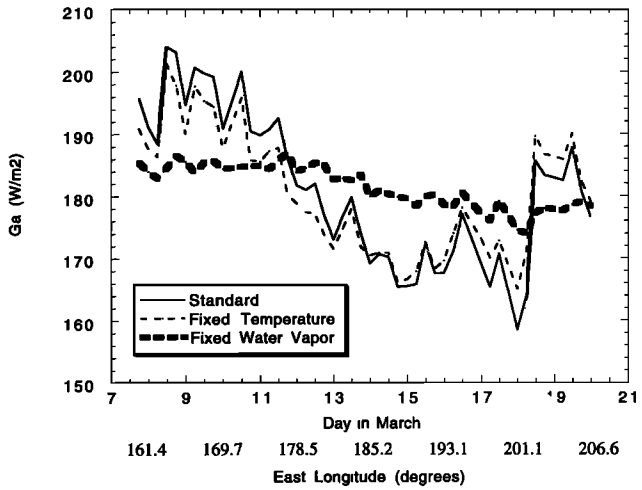

Figure 6. Total G_a along the ship track in W m^{-2} (equation (1)) calculated using the standard (solid curve), fixed temperature (thin dashed curve), and fixed water vapor (thick dashed curve) soundings.

March 15–16 in Figure 5 have low values of G_a characteristic of the surrounding clear points. As will be discussed below, 250 K represents a dividing line between two distinct populations of samples. Examining data taken along the ship track in the context of the satellite data gives us enough information to establish the connection among deep convection, water vapor, and G_a. Table 1 shows the mean column water vapor calculated for each of the two bins. The gradient from Table 1 is extremely similar to the inferred gradient from the time series along the ship track (Figures 3a and 3b). The gradient in 500- to 200-mbar water vapor in Table 1 is of the order of 150%. The balloon soundings indicated temperature changes at those pressures of the order of 0.5 K, which translates into purely thermodynamic changes of the order of less than 10%. Clearly, large increases in relative humidity are associated with the areas of deep convection.

4. Greenhouse Effect, Surface Fluxes and Heating Tendency

Greenhouse Effect

The radiation calculations show considerable variation of the order of 30–40 W m^{-2} in G_a along the ship track (solid curve in Figure 6). The total range in G_a brackets the mean value of 184 W m^{-2} obtained by *Inamdar and Ramanathan* [1994] for soundings above the threshold temperature for deep convection. Table 2 shows mean values of all the greenhouse effect calculations for GMS brightness temperatures less than 250 K and GMS brightness temperatures greater than or equal to 250 K. For soundings associated with a brightness temperature of less than 250 K, the mean G_a is 189.4 W m^{-2}. For soundings associated with a brightness temperature of 250 K or greater, the mean G_a is 171.9 W m^{-2}. Thus the difference in G_a between the two regimes is 17.5 W m^{-2}.

The results of three calculations of G_a are shown in Figure 6 using the standard, fixed temperature and fixed water vapor soundings, respectively. By using the fixed temperature soundings, one eliminates variability in G_a due to variability in atmospheric temperatures and SST. By using the fixed water vapor soundings, one eliminates variability in G_a due to variability in water vapor. The gradient in G_a from Table 2 of 15.0 W m^{-2} calculated using the fixed temperature soundings is 86% of the gradient in G_a calculated using the standard set of soundings. In other words, most of the total gradient is due to changes in water vapor alone, independent of changes in SST and $T(z)$. One can compare G_a in Figure

Table 1. Column-Integrated Water Vapor for the Total Column, and Lower, Middle, and Upper Troposphere, Binned by GMS Infrared Window Channel Brightness Temperature

Column Water Vapor	GMS T < 250 K	GMS T >= 250 K
Total column	49.9 kg m^{-2}	39.4 kg m^{-2}
Surface to 850 mbar	22.4 kg m^{-2}	21.0 kg m^{-2}
850 to 500 mbar	23.5 kg m^{-2}	16.8 kg m^{-2}
500 to 200 mbar	4.0 kg m^{-2}	1.6 kg m^{-2}

Numbers represent the mean of all the soundings in a temperature bin. All values are in kilograms per meter (kg m^{-2}).

Table 2. Summary of G_a Calculations for the Three Cases Using the Standard, Fixed Temperature, and Fixed Water Vapor Soundings, Binned by GMS Infrared Window Channel Brightness Temperature

	G_a	G_{low}	G_{mid}	G_{up}
	Standard Soundings			
GMS T < 250	189.4	44.7	75.7	57.4
GMS T >= 250	171.9	40.5	69.5	50.2
	Fixed T Soundings			
GMS T < 250	187.5	43.1	75.9	57.6
GMS T >= 250	172.5	42.0	69.1	50.1
	Fixed W Soundings			
GMS T < 250	182.8	44.1	72.4	55.3
GMS T >= 250	180.4	40.9	73.1	55.3

Numbers represent the mean of all soundings in a temperature bin. All values are in watts per square meter (W m^{-2}).

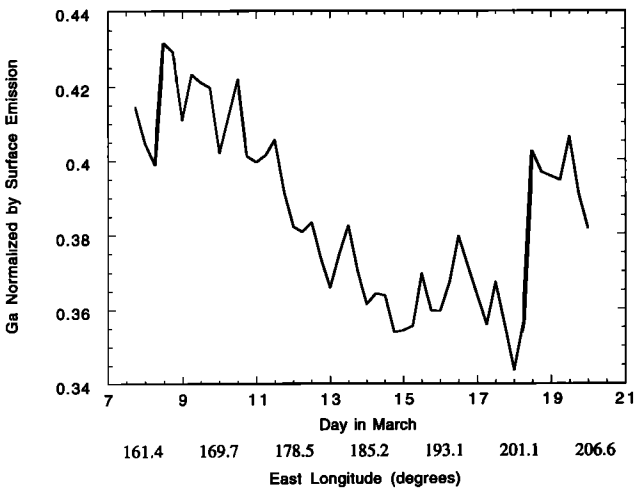

Figure 7. Total G_a normalized by surface emission calculated using the standard soundings.

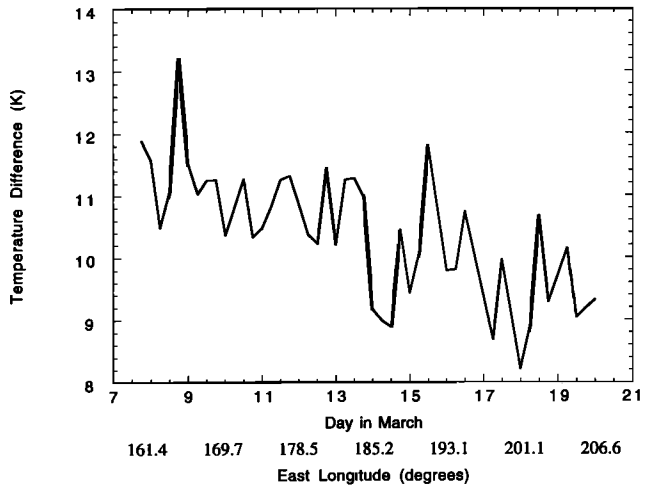

Figure 9. Difference between SST and 850-mbar temperature in K along the ship track.

6 to column water vapor shown in Figure 3a and 3b and Table 1. The gradient in fixed water vapor G_a from Table 2 is 2.4 W m^{-2}. These results indicate that a similar strong statistical correlation between water vapor and G_a (or quantities similar to G_a) from monthly average observations [*Raval and Ramanathan*, 1989; *Stephens and Greenwald*, 1991; *Webb et al.*, 1993] holds on much shorter timescales. In an alternative presentation, Figure 7 shows G_a normalized by surface emission (σSST^4). This approximately eliminates the contribution of $\partial G_a/\partial$(SST). The two groups of points with elevated normalized G_a at the western and eastern edges of the ship track are those associated with deep convection (low OLR and low GMS infrared brightness temperatures).

Lower troposphere G_a is shown in Figure 8 for the cases standard, fixed temperature, and fixed water vapor. In a similar manner to (1) we can define G_a for a given layer in the atmosphere by the following:

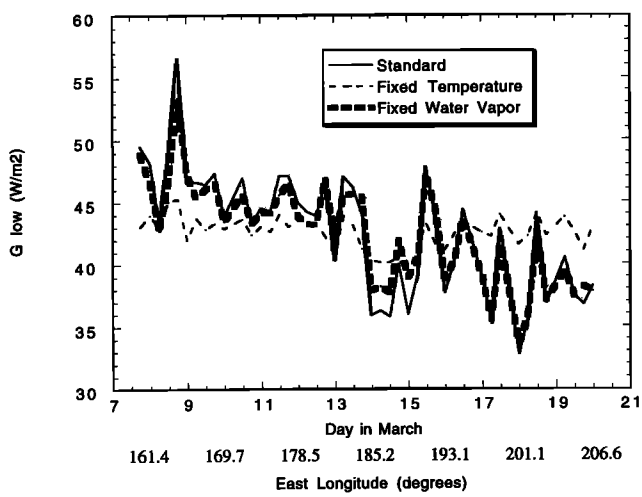

Figure 8. Surface to 850 mbar G_a (G_{low}) along the ship track in W m^{-2} (equation (4)) calculated using the standard (solid curve), fixed temperature (thin dashed curve), and fixed water vapor (thick dashed curve) soundings.

$$G_i = F_i^+ - F_{i+1}^+ \quad (4)$$

In this case, F_i^+ is the upwelling flux at the base of the layer and F_{i+1}^+ is the upwelling flux at the top of the layer. The lower troposphere contributes 4.2 W m^{-2} to the gradient in total column G_a calculated using the standard set of soundings (Table 2). In a reversal of the situation for the total atmospheric column we see that the fixed water vapor case reproduces most of the variability of the standard case (3.2 W m^{-2}), while fixing the temperature profile eliminates most of the gradient, reducing it to 1.1 W m^{-2}. This is due primarily to the small variation in column water vapor in the lower troposphere and the change in surface emission due to the west-to-east gradient in SST. We find little variation of water vapor below 850 mbar due to changes in surface temperature. Thus we see that lapse rate changes are important in the lower troposphere, in agreement with *Inamdar and Ramanathan* [1994]. As the SST increases, we find that temperature changes immediately above the boundary layer remain small (Figure 9). This results in an increase in the lower-level lapse rate with SST and an enhancement of the longwave trapping. *Wallace* [1992] and *Lindzen and Nigam* [1987] have noted that tropical atmospheric temperatures above the boundary layer are relatively homogeneous over large longitudinal areas.

From Table 2 we see that the middle troposphere contributes 6.2 W m^{-2} to the gradient in total column G_a calculated using the standard set of soundings (also see Figure 10). Recall that in Table 1, the middle troposphere column water vapor gradient was 6.7 kg m^{-2}. It is notable that even with most of the absolute column water vapor change in the middle troposphere, changes in the 850- to 500-mbar G_a only account for 35% of the total column gradient in G_a. The troposphere below 500 mbar contributes 59% to the total gradient in G_a.

The variation in G_a in the upper troposphere is clearly dominated by changes in q (Figure 11). Table 2 shows a G_a gradient of 7.2 W m^{-2}, 41% of the total atmospheric change. Furthermore, G_a from 500 to 200 mbar represents 50% of the total column gradient due to changes in water vapor alone (the fixed temperature case). This gradient is due to a systematic decrease in upper troposphere water vapor of ~2.5 kg m^{-2} from soundings associated with GMS

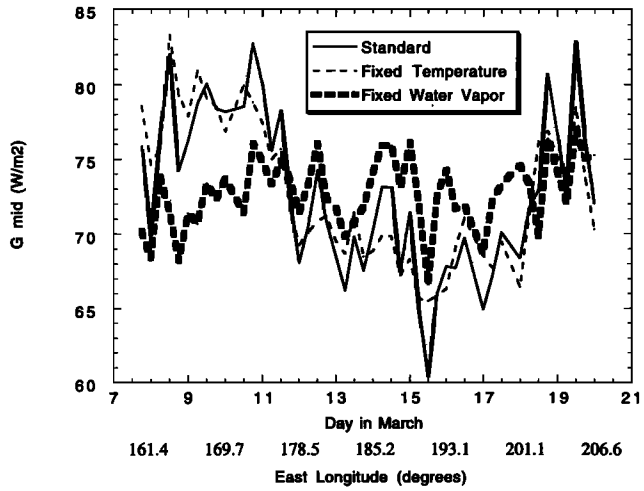

Figure 10. 850- to 500-mbar G_a (G_{mid}) along the ship track in W m^{-2} (equation (4)) calculated using the standard (solid curve), fixed temperature (thin dashed curve), and fixed water vapor (thick dashed curve) soundings.

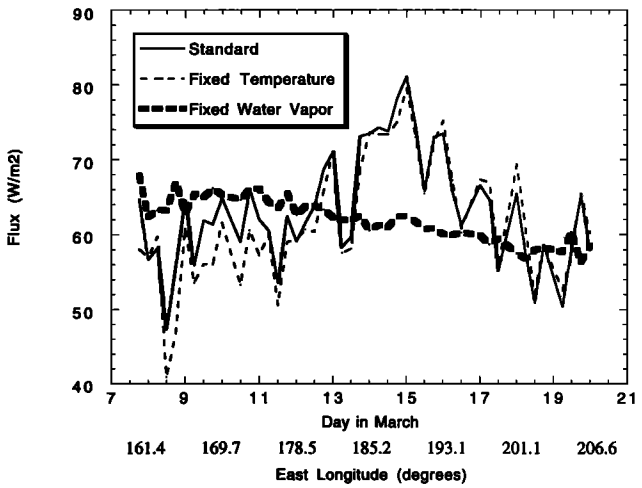

Figure 12. Surface net flux (upwelling minus downwelling) along the ship track in W m^{-2} calculated using the standard (solid curve), fixed temperature (thin dashed curve), and fixed water vapor (thick dashed curve) soundings.

brightness temperatures less than to greater than 250 K (recall Table 2). The fixed water vapor curve shows essentially no trend across the CEPEX region. A small absolute change in upper troposphere water vapor (but a large percentage change) leads to a large change in G_a. This enhanced trapping is due to the emission of radiation from water vapor at the low temperatures characteristic of the upper troposphere [*Liou*, 1980]. Thus the largest contributor to the rapid rise in G_a from clear to cloudy regions is a significant moistening of the troposphere between 500 and 200 mbar. In section 3 we discussed the correspondence between the observed upper tropospheric moisture field and the prevalence in space and time of deep convective events. *Betts* [1990] and *Sun and Lindzen* [1993] suggest that deep convection leads to moistening of the upper troposphere due to evaporation and dissipation of cirrus anvils associated with cumulonimbus towers.

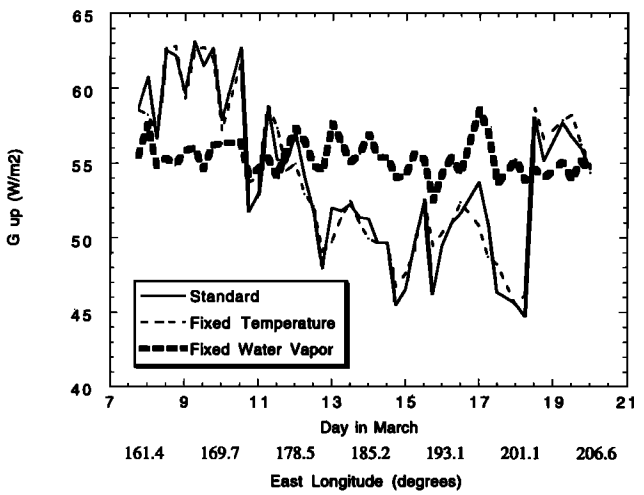

Figure 11. 500- to 200-mbar G_a (G_{up}) along the ship track in W m^{-2} (equation (4)) calculated using the standard (solid curve), fixed temperature (thin dashed curve), and fixed water vapor (thick dashed curve) soundings.

Fluxes and Atmospheric Heating Tendency

The net longwave flux at the surface is important in the surface energy balance. One can also use upwelling and downwelling fluxes in the atmosphere to determine the amount of radiative energy a given layer is gaining or losing. Figure 12 shows a broad increase in surface net flux from west to east until approximately 190°E, followed by a decrease to the edge of the sampling region. This general trend agrees with in situ measurements onboard the R/V *Vickers* from a high-precision Fourier transform infrared spectroradiometer [*Lubin*, 1993]. The surface emission decreases as the temperature decreases from west to east. This is visible in the fixed water vapor curve of Figure 12, indicating that water vapor changes are responsible for most of the variability in downward flux at the surface. The additional downwelling flux at the surface is due to increases in water vapor below 700 mbar. The sharp minimum in downward flux (and consequently the maximum in net flux) corresponds to minima in the lower and middle troposphere column water vapor (Figure 3a). One can observe from these calculations that moving from 160°E until 190°E, the decrease in surface downward flux exceeds the decrease in surface upward flux leading to an overall increase in net flux. East of approximately 190°E the combination of decreased surface emission and increased water vapor concentration below 700 mbar cause the surface net flux to decrease again. If we bin the surface flux calculations by GMS brightness temperature in the same way as the greenhouse effect calculations (Table 3), we find a cloudy-to-clear gradient in net flux of −6.6 W m^{-2} and in downward flux of 9.0 W m^{-2}. Following *Ramanathan and Collins* [1991] and *Inamdar and Ramanathan* [1994] it becomes more difficult for the surface to cool radiatively as SST increases. The heating of the entire column is given by

$$H = G_a - F_{surf}^{-} \tag{5}$$

where F_{surf}^{-} is the downwelling flux at the surface. This is a negative quantity, so there is a net radiative cooling of the atmosphere. The increase in downward flux of 9.0 W m^{-2} is

Table 3. Surface Net Flux and Surface Downwelling Flux Binned by GMS Infrared Window Channel Brightness Temperature

Flux Quantity	GMS $T < 250$ K	GMS $T >= 250$ K
Net flux at surface	60.2 W m^{-2}	66.8 W m^{-2}
Surface emission	470.4 W m^{-2}	468.1 W m^{-2}
Down flux at surface	410.3 W m^{-2}	401.3 W m^{-2}

Numbers represent the mean of all calculations over the particular group of soundings. All values are in W m^{-2}.

smaller than the increase in G_a (17.5 W m^{-2} from the previous section). Thus there is a reduced atmospheric radiative cooling of 8.5 W m^{-2} in the convective regime compared to the nonconvective regime.

Figures 13a–13c show the heating tendency for the lower, middle, and upper troposphere. We define heating tendency of a layer as follows:

$$H_i = G_i + (F_{i+1}^{-} - F_i^{-}) \quad (6)$$

G_i is the greenhouse trapping of a given atmospheric layer (equation (2)). F_{i+1}^{-} and F_i^{-} represent the downwelling flux at the top and bottom of the layer, respectively. We expect H_i to be negative in the troposphere (cooling). Larger negative values indicate increased cooling. One can immediately identify two points: first, the gradient in H is more strongly dependent on water vapor than temperature changes in all three layers (e.g., the fixed temperature versus the fixed water vapor curve in Figures 13a–13c); second, Figures 13a–13c show broad decreases in cooling under convective conditions in the lower and middle troposphere but a clear increase in the upper troposphere. The additional upper level water vapor in the convective regime produces strong cooling above 500 mbar with a total gradient from convective to nonconvective areas of approximately 30 W m^{-2}. Below 500 mbar the increase in G_a under cloudy skies combines with a corresponding increase in the downward flux into the layer, overbalancing the increase in downward flux out of the layer and reducing cooling. This is interesting in light of *Inamdar and Ramanathan*'s [1994] finding that atmospheric cooling is greater at all altitudes in the convective regime compared to the nonconvective regime. In this study, the greatly increased opacity above 500 mbar in the convective regime produces a large downwelling flux which heats the levels below. It is possible that the cooling of the upper troposphere and the heating of the lower stimulates additional deep convective events by destabilizing the atmospheric column and contributes to the persistence of synoptic-scale deep convection in a particular region.

5. Summary and Discussion

This work is an extension of previous studies which considered radiation and water vapor interactions in climatologically convective and nonconvective oceans. The entire region under investigation can be considered climatologically convective with SST everywhere greater than 300 K (and mostly greater than 301 K). This inference is borne out by observations of active deep convection both in the warmer, western half of the CEPEX region and in the predominantly clear eastern half toward the end of the sampling period (Figures 4 and 5).

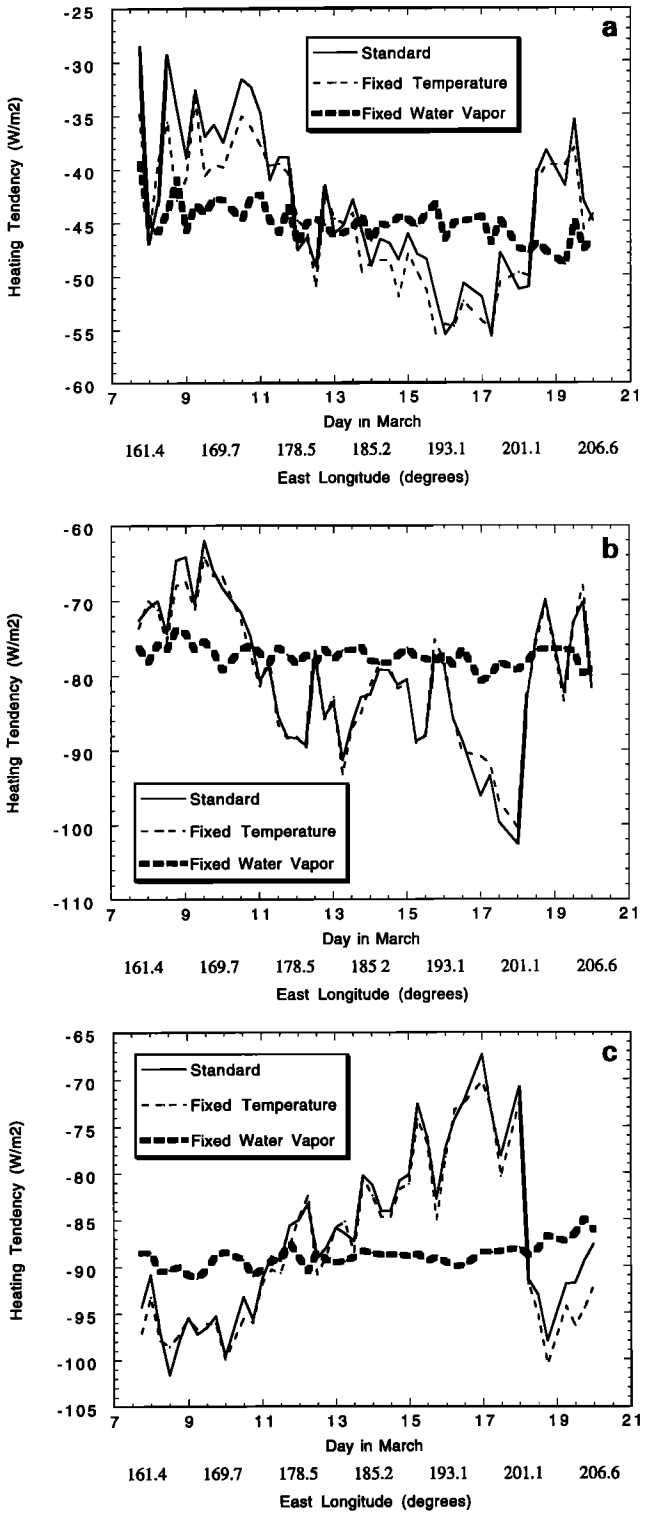

Figure 13. (a) Heating tendency along the ship track in W m^{-2} (equation (6)) in the layer surface to 850 mbar calculated using the standard (solid curve), fixed temperature (thin dashed curve), and fixed water vapor (thick dashed curve) soundings. (b) Same as Figure 13a but for the layer 850 to 500 mbar. (c) Same as Figure 13a but for the layer 500 to 200 mbar.

Lower-level water vapor mixing ratio and low-level column-integrated water vapor show little variation from west to east, or little thermodynamic variation with SST. Middle and upper level column-integrated water vapor show large gradients, decreasing significantly in clear-sky conditions. These gradients are much larger than expected changes due only to temperature in a fixed relative humidity system.

Colocated NMC OLR analyzed fields and satellite observations show active deep convection in the areas with high G_a and generally clear, suppressed conditions in the areas with low trapping. At the end of the sampling period the ship sailed into a region of convection in the previously clear ocean (Figures 4 and 5). The effects of convection are easily seen in the strong rise in G_a and upper tropospheric water vapor (soundings 41–45 in Figures 3b, 6, and 7).

Total atmospheric column G_a and particularly 500- to 200-mbar G_a show large variation and a general increase under convective conditions. The 500- to 200-mbar G_a represents approximately 41% of the total gradient, due to significant moistening of convective soundings above 500 mbar. By fixing the water vapor and temperature profiles in turn for each sounding, we find that 86% of the gradient in total G_a and 100% of the gradient in 500- to 200-mbar G_a is due to the gradient in water vapor alone, independent of changes in the temperature profile. In the lower troposphere from the surface to 850 mbar the west-to-east variation in G_a can be explained largely by a steepening of the lapse rate near the surface as the SST increases toward the west. Above 850 mbar the atmosphere is relatively homogeneous in temperature (recall Figure 9).

Though the difference in G_a between the soundings with GMS brightness temperatures less than 250 K and those with brightness temperatures greater than or equal to 250 K is 17.5 W m^{-2}, the corresponding difference in downwelling flux at the surface is only 9.0 W m^{-2}, indicating a decreased radiative cooling of the atmosphere in the region associated with deep convection. This effect has been modeled by *Minschwaner and McElroy* [1992]. The results indicate that G_a increases due to upper tropospheric moistening by deep convective events. The corresponding effect on F^-_{surf} is less since the tropical atmosphere is optically thick, and F^-_{surf} is dominated by the temperature and humidity profile near the surface.

There is a pronounced increase in cooling above 500 mbar in the west compared to the east due to enhanced water vapor concentration. This contrasts with decreased cooling in the middle and lower troposphere in the deep convective regime. This would tend to destabilize the column in regions of deep convection and could indicate a feedback that allows deep convection to persist. This study ignores the effect of clouds, however, which could alter the magnitude and even the sign of the inferred feedback.

Figure 14 is a summary of the results of this study in the form of a phase diagram of G_a as a function of SST and mean GMS infrared brightness temperature. The mean brightness temperature is just that described in section 3 and Figure 5. We consider clear skies to be those with a mean brightness temperature at least 280 K. The CEPEX observations have allowed us to fill in parts of the diagram: in particular, clear skies at all SSTs and cloudy skies at SSTs above 302 and around 300.5 K. G_a varies along both axes. The variation along the SST axis for clear skies agrees well with aircraft radiometer measurements taken during CEPEX [*Valero et al.*, 1993]. For mean brightness temperatures above 280 K the variation is due to the change in surface emission associated with an SST range of ~2 K and also to changes in water vapor concentration above 850 mbar. The variation in mixing ratio is much larger than can be explained by purely thermodynamic changes since the temperature is quite uniform. By recalculating the phase diagram with the fixed temperature and fixed water vapor profiles, we find that the relative magnitudes of the SST and water vapor effects are approximately equal. In contrast, the variation along the brightness temperature axis is due almost entirely to variations in water vapor. Note that the bin bounded by SSTs of 301 and 301.5 K and brightness temperatures of 250 and 260 K is associated with the anomalous cloudy points on March 15–16 (Figure 5). These appear to be associated with high (cold) cloud but not necessarily with active deep convection.

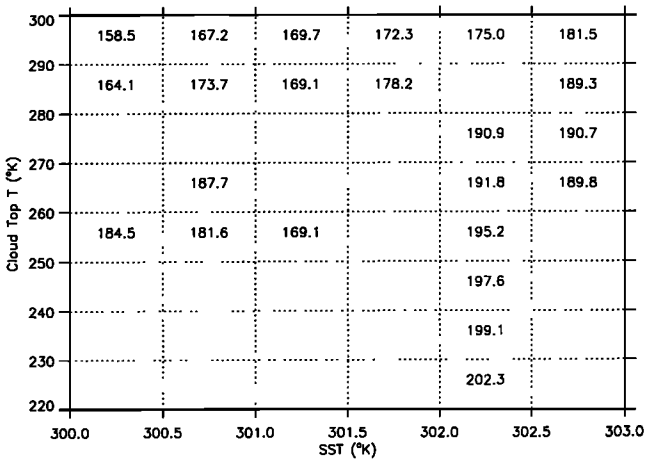

Figure 14. Phase diagram of G_a (W m^{-2}) in SST and mean GMS infrared brightness temperature space.

From this and previous studies it seems clear that deep convection decreases outgoing longwave radiation both through cloud longwave forcing and through its association with upper tropospheric moistening. It is worthwhile to point out that we consider a sample in which all the soundings are potentially convective, while *Inamdar and Ramanathan* [1994] compare soundings between climatologically convective and nonconvective regimes. We can extend their mechanism for the supergreenhouse effect in the following manner. In the transition from climatologically nonconvective to climatologically convective regimes, G_a increases with SST due to a steepening of the lapse rate at all levels and due to increasing water vapor concentrations in the lower and lower-middle troposphere following the increase in temperature. Once the threshold temperature for deep convection is passed, lapse rate steepening remains important only in the lower troposphere below approximately 850 mbar. Since lower tropospheric water vapor becomes nearly constant, sharp increases in G_a come from increases in upper level water vapor due to deep convection.

We may restate the key issue as follows: In the CEPEX sample, when SST reaches the threshold temperature for deep convection, large changes in G_a at fixed SST are associated with synoptic-scale deep convective events. In this paper we have examined the variation of G_a with convection. The total derivative of G_a with SST depends on

a statistical correlation between the SST and the frequency of deep convection. *Waliser et al.* [1993], using satellite observations, and *Zhang* [1993] have shown a correlation between higher SST and increasing deep convection in the temperature range for deep convection. The space and timescales on which this relationship holds is crucial to determining the nature of the supergreenhouse effect in the tropics.

Acknowledgments. This work was supported in part by the NSF Science and Technology Center for Clouds, Chemistry and Climate (C^4) as well as by the Federal Ministry for Research and Technology of Germany. It represents C^4 paper number 106. The Central Equatorial Pacific Experiment was funded by NSF and DOE. We would like to thank the National Center for Atmospheric Research for providing the OLR and SST data. We would like to thank an anonymous reviewer for helpful comments and suggestions. We would also like to thank D. Lubin, S. Sherwood, A. Inamdar, and V. Ramanathan for useful discussions. Finally, we would like to thank B. Bernstein and the staff of SeaSpace for their help in obtaining the GMS 4 data.

References

Betts, A. K., Greenhouse warming and the tropical water budget, *Bull. Am. Meteorol. Soc.*, *71*(10), 1464–1465, 1990.

Dutton, E. G., An extended comparison between LOWTRAN7 computed and observed broadband thermal irradiances: Global extreme and intermediate surface conditions, *J. Atmos. Oceanic Technol.*, *10*, 326–336, 1993.

Ellingson, R. G., J. S. Ellis, and S. B. Fels, The intercomparison of radiation codes used in climate models: Longwave results, *J. Geophys. Res.*, *96*(D9), 8929–8953, 1991.

Gadgil, S., P. V. Joseph, and N. V. Joshi, Ocean-atmosphere coupling over monsoon regions, *Nature*, *312*, 141–143, 1984.

Graham, N. E., and T. P. Barnett, Sea surface temperature, surface wind divergence, and convection over tropical oceans, *Science*, *238*, 657–659, 1987.

Hallberg, R., and A. K. Inamdar, Observations of seasonal variations in atmospheric greenhouse trapping and its enhancement at high sea surface temperature, *J. Clim.*, *6*(5), 920–931, 1993.

Inamdar, A. K., and V. Ramanathan, Physics of greenhouse effect and convection in warm oceans, *J. Clim.*, *7*(5), 715–731, 1994.

Kiehl, J. T., and B. P. Briegleb, Comparison of the observed and calculated clear sky greenhouse effect: Implications for climate studies, *J. Geophys. Res.*, *97*(D9), 10,037–10,049, 1992.

Kley, D., H. Voemel, H. Grassl, V. Ramanathan, S. C. Sherwood, and S. F. Williams, Cross section of tropospheric water vapor during CEPEX between 160 degrees east and 160 degrees west, *Eos Trans. AGU*, *74*(43), Fall Meeting suppl., 115, 1993.

Kneizys, F. X., E. P. Shettle, L. W. Abreu, J. H. Chetwynd, G. P. Anderson, W. O. Gallery, J. E. A. Selby, and A. A. Clough, Users Guide to Lowtran 7, *Tech. Rep. AFGL-TR-88-0177*, 137 pp., Air Force Geophys. Lab., Hanscom Air Force Base, Mass., 1988.

Lindzen, R. S., and S. Nigam, On the role of sea surface temperature gradients in forcing low-level winds and convergence in the tropics, *J. Atmos. Sci.*, *44*, 2418–2435, 1987.

Liou, K. N., *An Introduction to Atmospheric Radiation*, 392 pp., Academic, San Diego, Calif., 1980.

Lubin, D., FTIR determination of the tropical supergreenhouse effect during CEPEX, *Eos Trans. AGU*, *74*(43), Fall Meeting suppl., 115, 1993.

Manabe, S., and R. T. Wetherald, Thermal equilibrium of the atmosphere with a given distribution of relative humidity, *J. Atmos. Sci.*, *24*, 241–259, 1967.

Minschwaner, K., and M. B. McElroy, A model for the energy budget of the atmosphere: Comparison with data from the Earth Radiation Budget Experiment, *Planet. Space Sci.*, *40*(9), 1237–1250, 1992.

Ramanathan, V., and W. Collins, Thermodynamic regulation of ocean warming by cirrus clouds deduced from observations of the 1987 El Nino, *Nature*, *351*, 27–32, 1991.

Raval, A., and V. Ramanathan, Observational determination of the greenhouse effect, *Nature*, *342*, 758–761, 1989.

Reynolds, R. W., A real-time global sea surface temperature analysis, *J. Clim.*, *1*, 75–86, 1988.

Rind, D., E. W. Chiou, W. Chu, J. Larsen, S. Oltmans, J. Lerner, M. P. McCormick, and L. McMaster, Positive water vapor feedback in climate models confirmed by satellite data, *Nature*, *349*, 500–503, 1991.

Shine, K. P., and A. Sinha, Sensitivity of the Earth's climate to height-dependent changes in the water vapour mixing ratio, *Nature*, *354*, 382–384, 1991.

Slingo, A., and M. J. Webb, Simulation of clear-sky outgoing longwave radiation over the oceans using operational analyses, *Q. J. R. Meteorol. Soc.*, *118*, 1117–1144, 1992.

Stephens, G. L., and T. J. Greenwald, The Earth's radiation budget and its relation to atmospheric hydrology, 1, Observations of the clear sky greenhouse effect, *J. Geophys. Res.*, *96*(D8), 15,311–15,324, 1991.

Sun, D., and R. S. Lindzen, Distribution of tropical tropospheric water vapor, *J. Atmos. Sci.*, *50*(12), 1643–1660, 1993.

Valero, F. P. J., P. Pilewskie, and A. Bucholtz, Determination of the clear-sky greenhouse trapping of infrared radiation from multi-level aircraft measurements over the central equatorial Pacific, *Eos Trans. AGU*, *74*(43), Fall Meeting Suppl., 107, 1993.

Waliser, D. E., N. E. Graham, and C. Gautier, Comparison of the highly reflective cloud and outgoing longwave radiation datasets for use in estimating tropical deep convection, *J. Clim.*, *6*, 331–353, 1993.

Wallace, J. M., Effect of deep convection on the regulation of tropical sea surface temperature, *Nature*, *357*, 230–231, 1992.

Webb, M. J., A. Slingo, and G. L. Stephens, Seasonal variations of the clear-sky greenhouse effect: The role of changes in atmospheric temperatures and humidities, *Clim. Dyn.*, *3*, 117–129, 1993.

Zhang, C., Large-scale variability of atmospheric deep convection in relation to sea surface temperature in the tropics, *J. Clim.*, *6*, 1898–1913, 1993.

W. D. Collins and C. P. Weaver, Center for Clouds, Chemistry and Climate, Scripps Institution for Oceanography, La Jolla, CA 92093.

H. Grassl, Max Planck Institute for Meteorology, Mainz, Germany.

(Received March 15, 1994; revised August 16, 1994;
accepted August 24, 1994.)